Full length article

On the crystallography and composition of topologically close-packed phases in ATI 718Plus®

Robert Krakow [a],[*], Duncan N. Johnstone [a], Alexander S. Eggeman [a], Daniela Hünert [b], Mark C. Hardy [c], Catherine M.F. Rae [a], Paul A. Midgley [a]

[a] Department of Materials Science and Metallurgy, University of Cambridge, 27 Charles Babbage Road, Cambridge, CB3 0FS, UK
[b] Rolls-Royce Deutschland Ltd. & Co KG, Eschenweg 11, 15827, Blankenfelde-Mahlow, Germany
[c] Rolls-Royce plc, PO Box 31, Derby, DE24 8BJ, UK

ARTICLE INFO

ABSTRACT

ATI 718Plus® is a nickel-based superalloy developed to replace Inconel 718 in aero engines for static and rotating applications. Here, the long-term stability of the alloy was studied and it was found that topologically close-packed (TCP) phases can form at the γ-η interface or, less frequently, at grain boundaries. Conventional and scanning transmission electron microscopy techniques were applied to elucidate the crystal structure and composition of these TCP precipitates. The precipitates were found to be tetragonal sigma phase and hexagonal C14 Laves phase, both being enriched in Cr, Co, Fe and Mo though sigma has a higher Cr and lower Nb content. The precipitates were observed to be heavily faulted along multiple planes. In addition, the disorientations between the TCP phases and neighbouring η/γ were determined using scanning precession electron diffraction and evaluated in axis-angle space. This work therefore provides a series of compositional and crystallographic insights that may be used to guide future alloy design.

© 2017 Acta Materialia Inc. Published by Elsevier Ltd. This is an open access article under the CC BY license (http://creativecommons.org/licenses/by/4.0/).

1. Introduction

The nickel-based superalloy ATI 718Plus® (hereafter 718Plus) has been developed with a view to replace the current workhorse alloy in the gas turbine industry, Inconel 718 (hereafter 718). This new alloy offers an operating temperature increase of about 37 K whilst maintaining workability and weldability [1]. This is achieved through changes in the alloy composition. Most importantly, the Al:Ti ratio is increased and W is added (Table 1), which leads to changes in precipitation behaviour within the γ matrix (Ni, Al, cubic, $Fm\bar{3}m$). In alloy 718 the primary strengthening phase responsible for increased dislocation drag is a fine dispersion of γ″ (Ni₃Nb, $D0_{22}$, tetragonal, $I4/mmm$) with some γ′ (Ni₃Al/Ti, $L1_2$, cubic, $Pm\bar{3}m$), whereas the main strengthening phase in 718Plus is γ′ [2] although some have argued that γ″ may still occur [3]. This is key to performance because γ′ is stable to higher temperatures than γ″, which readily transforms to δ phase above 650 °C [4,5]. The other major difference is that where the

dominant grain boundary precipitates in alloy 718 are needle-like δ phase (Ni₃Nb, $D0_a$, orthorhombic, $Pmmn$) the dominant precipitates in 718Plus are η phase (Ni₃Nb₀.₅(Al/Ti)₀.₅, $D0_{24}$, hexagonal, $P6_3/mmc$).

The morphology of η phase precipitates in 718Plus depends on the thermo-mechanical treatment to which the alloy has been subjected. Often it occurs in colonies in a Blackburn orientation relationship $\{111\}_\gamma \,||\{001\}_\eta$ [7] with one of the adjacent grains. The η phase precipitates then grow in a disc-like morphology on the $\{111\}_\gamma$ matrix planes towards the grain interior and a detailed mechanism has been suggested [8]. It is also common to observe small fractions of fine δ phase sheets within η phase discs [7,8]. In the context of this study it is important to note that after prolonged annealing η precipitates can grow significantly in size, spanning across entire grains as well as growing in aspect ratio to form blocky precipitates with distinct facets [9]. Further, both η and γ′ compete for the same alloying elements, mainly Al, Ti and Nb, resulting in γ′ precipitate free zones (PFZ) around η precipitates and the suggestion that γ′ might play a role in the formation of η [10]. Considering mechanical performance, the η phase is critical for effective grain boundary pinning in sub-solvus forging [11–13] and whether, for example, fine or blocky

* Corresponding author.
  E-mail address: rk471@cam.ac.uk (R. Krakow).

Table 1
Composition of ATI 718Plus and Inconel 718 in wt% [6,7].

Element wt%	Al	Ti	Cr	Fe	Co	Ni	Nb	Mo	W	C + B + P
718Plus	1.45	0.7	18.0	10.0	9.0	Bal.	5.4	2.7	1.0	<0.05
Inconel 718	0.45	1.0	18.1	18.0	—	Bal.	5.4	2.9	—	<0.05

precipitates have formed, and to what extent, will have a strong effect on mechanical properties [9].

Topologically close-packed (TCP) phases may form in most nickel-based superalloys [14,15] when exposed to conditions of high temperature for long periods of time or during solidification and welding [16–18]. Typically, TCP phases are composed principally of the elements Ni, Cr, Co, Mo, and W, and the basic crystallography of common TCP phases is summarised in the supplementary information (Table SI 1). The structures are relatively complex [19,20] but at the simplest level consist of pseudo-hexagonal layers of atoms stacked to form sites with coordination numbers as high as 16 accommodating atoms of widely different sizes. In spite of this, the packing efficiencies are comparable to those of ideal close-packed structures. The TCP phases are potentially detrimental if they occur in significant volume fractions such as to cause the depletion of solute atoms which otherwise aid solid solution strengthening [21]; they cannot be used as strengthening phases themselves due to low number density [22].

The occurrence of TCP phases in 718Plus has so far been little studied and those studies that do report TCP phases [6,16,18,23] in 718Plus have largely neglected their crystallography. Instead, the TCP phases have been identified based mainly on composition, which makes it unclear as to exactly which TCP phases are observed. In terms of the conditions leading to the observation of TCP phases in 718Plus this has mostly been attributed to solidification of the alloy after casting [6] or to welding [16,18,23]. Interestingly, we note that no TCP phases were reported in a study on long term stability of 718Plus (732 °C, 2500 h) by Radavich et al. [24]. In this work, we report the observation of TCP phases in 718Plus subjected to high temperature annealing and characterise TCP precipitates both chemically and crystallographically using (scanning) transmission electron microscopy and diffraction.

2. Methods

2.1. Heat treatments

718Plus samples were provided by Rolls-Royce Deutschland Ltd. & Co KG. The initial ingot material was triple vacuum melted by Allegheny Technologies Inc. for high cleanliness and forged into billet product. This was followed by subsolvus forging to form a black forging and heat treatment A (Table 2) performed by Otto Fuchs KG. Further, long-term anneals B-D were performed by the authors, on separate samples, in order to examine microstructural stability.

Table 2
718Plus samples investigated, with details of respective heat treatment.

Treatment	Details	Treatment	Details
A	843-871 °C for 16 h	+B	+650 °C for 500 h
	954-982 °C for 1 h	+C	+704 °C for 500 h
	788 °C/8 h/FC + 704 °C/8 h	+D	+788 °C for 500 h

2.2. Specimen preparation

Electron-transparent thin film specimens were prepared as follows. First, samples were extracted from the mid-radius of the heat-treated forgings using electric discharge machining (EDM). Slices of 300−500 μm were cut using a saw and 3 mm diameter discs were produced using EDM. These discs were ground to approximately 200 μm thickness and subjected to electrolytic twin-jet polishing using a Tenupol and 10 vol% perchloric acid solution at −5 °C.

2.3. (Scanning) transmission electron microscopy

TEM images and small angle convergent beam electron diffraction (CBED) patterns were acquired using Philips CM30 and JEOL 200CX microscopes operated at 200 kV. Most images and diffraction patterns were acquired using Gatan 2K digital cameras (Orius SC200) although selected images were acquired on photographic film.

Scanning transmission electron microscopy (STEM) was performed using an FEI Tecnai Osiris. The machine was operated at 200 kV and energy dispersive X-ray (EDX) spectrum images and annular dark-field (ADF) images were acquired simultaneously using a scan step size of 3 nm. The specimen was not tilted and the gun lens was adjusted to produce a large current (0.7 nA) for increased X-ray generation, which allowed a modest 200−250 ms dwell time per pixel.

Scanning precession electron diffraction (SPED), in which a PED pattern is acquired at every position in a scan, was performed on a Philips CM300 FEGTEM operated at 300 kV. The scan and simultaneous precession of the electron beam was controlled using a NanoMegas Digistar system, combined with the ASTAR software package [25]. A convergent probe was used, typically with a convergence semi-angle ca. 1 mrad and a precession angle ca. 9 mrad, aligned as described recently [26]. Scans were acquired with a step size of 10 or 20 nm depending on the region of interest. The PED patterns were recorded using a Stingray CCD camera to capture the image on the binocular viewing screen with an exposure time of 40−60 ms. The recorded patterns were corrected for geometric distortions prior to any further analysis.

3. Results

3.1. The occurrence of TCP phases

TCP precipitates were observed in samples produced following all four heat treatments (A-D). In each sample, bright field (BF) images, as shown in Fig. 1, were obtained from approximately 20 TCP particles to assess sites of occurrence within the microstructure, their morphology and size. Across all samples, it was found that almost all (96%) occur at γ-η interfaces and often extend along specific η facets. In a number of cases, it appears that the TCP particles may have nucleated on an η precipitate and continued to grow towards a triple junction or along a grain boundary (e.g. Fig. 1b). TCP particles were also observed at some grain boundaries although it remains possible that these formed initially at a γ-η phase boundary, that was removed during TEM sample preparation. The particles are typically blocky in morphology and exhibit internal faulting. This is in contrast to other alloys in which the TCP particles are plate-like [19], may be a result of different misfit. In the as-received condition (A), particles were measured to have their largest dimension in the range 55−230 nm. After further annealing, the particles had grown size ranges: 50−320 nm, 80−1050 nm and 120−1170 nm for conditions B-D, respectively. In the remainder of this work, TCP precipitates are studied in sample D, which was
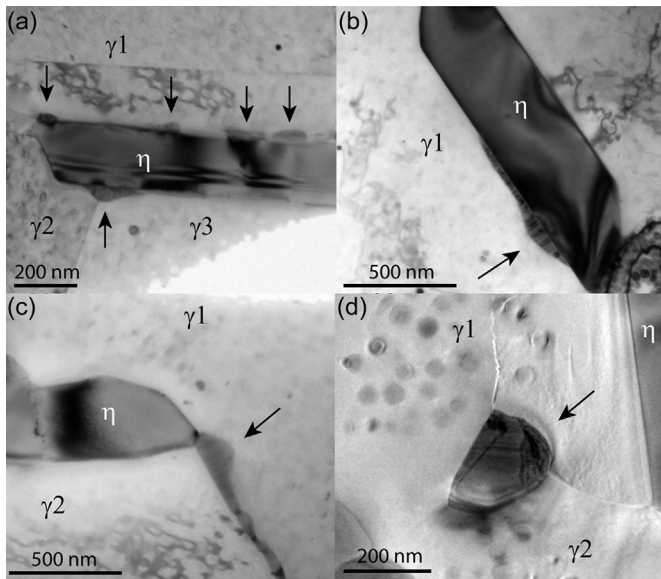
Fig. 1. BF images of (a) Five TCP particles at γ-η interface and (b) TCP particle at γ-η interface (c) TCP particle at γ-η interface extending along grain boundary (d) TCP phase at a grain boundary. TCP precipitates are arrowed.

produced following the highest temperature during the additional annealing step.

3.2. TCP phase identification by electron diffraction

Small angle CBED patterns were recorded at or near major zone axes of eight TCP precipitates and were assembled to illustrate their angular inter-relations within the stereogram (Fig. 2 and Fig. SI 1, 2). Phase identification was performed by indexation and comparison to simulated [27,28] kinematic electron diffraction patterns for known crystal structures (Table SI 2) noting that in some cases additional reflections were recorded due to multiple electron scattering events. In this way, it was determined that the structures of the TCP precipitates were consistent with those of the hexagonal

C14 Laves phase ($D0_{24}$, $P6_3/mmc$) or the tetragonal sigma (σ) phase (D_{4h}^{14}, $P4_2/mnm$). The lattice parameters were measured to be a = 4.9± 0.1 Å, c = 7.8± 0.1 Å for the C14 Laves phase and a = 8.8± 0.1 Å and c = 4.5± 0.1 Å for the sigma phase. It is noteworthy, that C14 has the same space group symmetry as η, the phase from which it appears to nucleate, though the cell parameters a and c are smaller by ca. 6%. The unit cells of the η phase and the identified TCP phases are shown in Fig. 3.

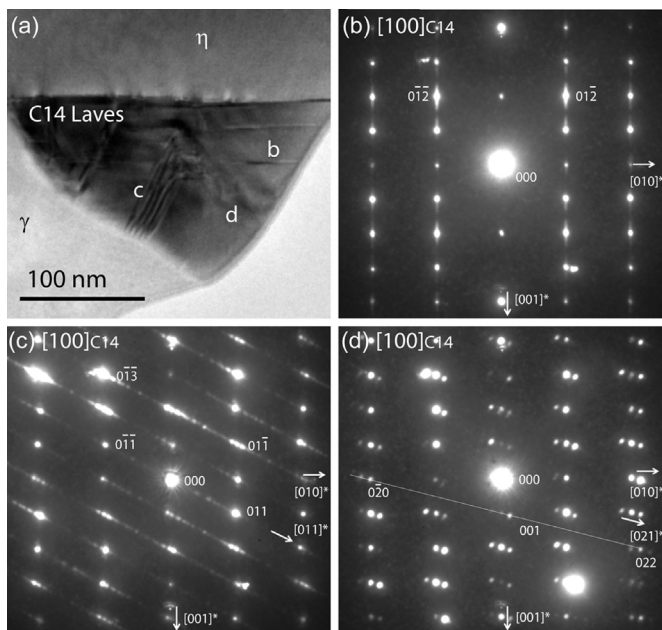### 3.3. Planar faults within C14 Laves

Planar faults are a common occurrence in TCP particles, especially Laves phase precipitates, and in the hexagonal polytypes the most common deformation process leading to these faults is the synchro-shear mechanism on the (001) basal plane [29]. This has been reported to lead to one set of parallel defect planes [30−33] with deformation on non-basal planes sparsely reported in C14 Laves although it may be possible at high temperature [34]. In this work, several sets of planar faults were observed in C14 Laves precipitates (Fig. 4 & Fig. SI3). This was investigated using small angle CBED with a beam diameter of ~20 nm to acquire diffraction patterns from the [100] zone axis in three different regions of the particle illustrating three observed behaviours (Fig. 4) as follows. In Fig. 4b streaking can be identified along the [001]* direction, especially near the $0\bar{1}2$ and the $01\bar{2}$ reflections consistent with the expected deformation mode for the hexagonal phase [35]. In Fig. 4c streaking occurs in the [011]* direction for example between the 000 and the 011 reflection. A closer look reveals that the streaking can be identified as many individual diffraction spots that span across the pattern. In Fig. 4d, distinct extra reflections are seen that appear to lie in the [021]* direction. Interestingly, there is no combined occurrence of any of the three phenomena in one diffraction pattern. The occurrence of faulting by modes other than basal plane deformation could be related to the large basal plane mismatch between C14 Laves and the η phase. Further, this clear evidence that non-basal plane faulting does occur after high-temperature annealing may be important for understanding high temperature stability and ductility in this alloy. It is also noted that in a number of images, faulting may be seen in σ phase precipitates
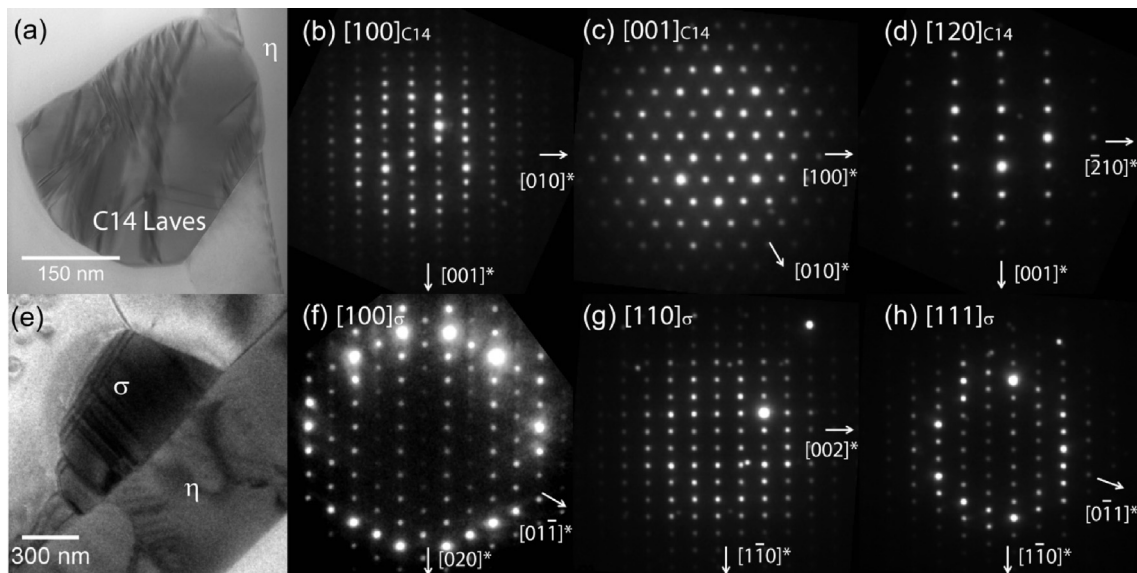
Fig. 2. (a) BF image of a C14 Laves phase particle (b−d) small angle CBED patterns at or near major zone axes of the hexagonal C14 Laves phase; (e) BF image of a σ phase particle (f−h) small angle CBED patterns at or near major zone axes of the tetragonal σ phase.
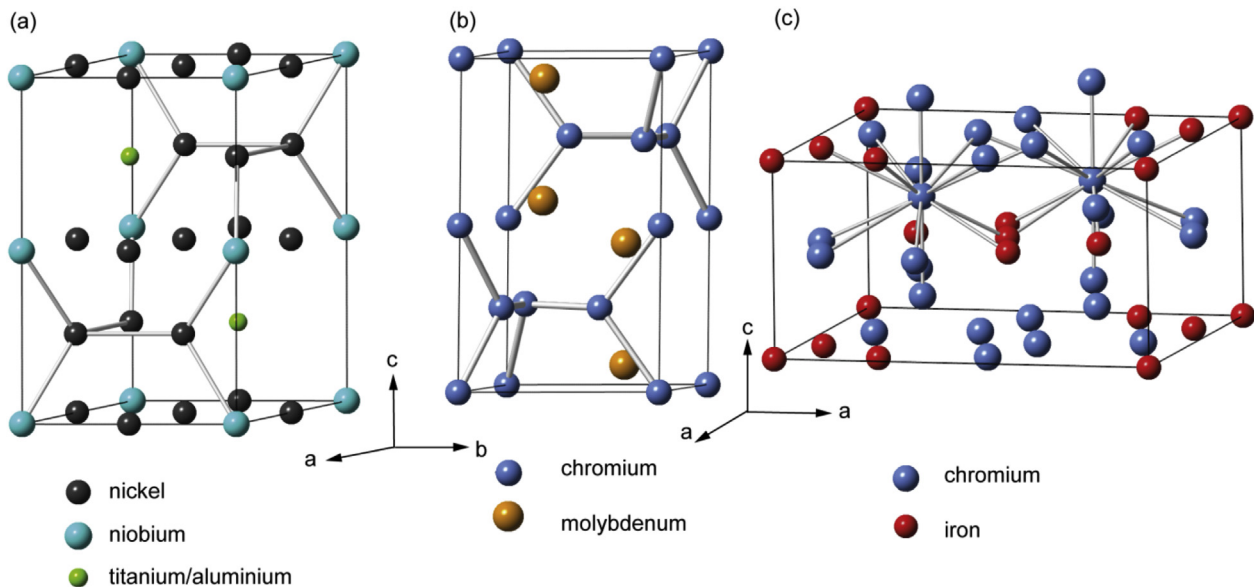
Fig. 3. Unit cells of the phases studied in this work. (a) η phase, (b) C14 Laves phase and (c) σ phase.

Fig. 4. (a): BF image of an η particle and adjacent C14 Laves phase with sets of planar faults; their basal planes join up at the interface (b–d) indexed diffraction patterns of different parts of the Laves phase taken at the same camera length parallel to the [100] zone axis.

on planes perpendicular to the σ-η interface e.g. Fig. 2 e.

3.4. TCP phase compositions

The composition of C14 Laves and σ phase precipitates was studied using STEM-EDX. Four C14 Laves phase, and two σ phase, precipitates were studied and an example of each, including elemental maps, is shown in Fig. 5. Cr, Fe, Co and Mo appear to partition strongly to both C14 Laves and σ phases compared to the η phase. Some elements (e.g. Ni) appear as though they may be enriched around the TCP precipitates; however, this increase in X-ray intensity is likely to be due to thickness variations in the

surrounding γ matrix and not chemical segregation. The phase compositions were determined using data processing methods implemented in the HyperSpy python library [36] as follows. The data was de-noised first using singular value decomposition and a mask based on the Mo-Kα X-ray line was used to isolate pixels within the TCP particles. Spectra associated with pixels in the particles were then summed to obtain a representative spectrum, which was modelled using a Gaussian peak at all relevant X-ray lines to extract accurate intensities. Cliff-Lorimer quantification [58] was then applied using k-factors obtained with respect to a Cu reference for the particular instrument used. The composition of each TCP precipitate obtained this way is shown in Table 3. The analysis shows an evident partitioning of Cr, Fe, Co and Mo and that both phases in this alloy contain small quantities of Al and Ti. C14 Laves phase shows ca. 5 at.% of Nb and W whereas the σ phase precipitates have significantly higher levels of Cr but very little Nb or W. The values obtained in this work for both C14 Laves and σ phases are self-consistent to within ±1 at.% and trends in enrichment appear consistent with values reported in the literature for TCP particles in 718 [37–39] (supplementary information, Table SI 3). It should be noted that the W concentration may be unreliable due to peak overlap but since it is a small contribution this has a small effect on the other values.

3.5. Crystallographic orientation relationships

C14 Laves and σ phase precipitates were primarily observed adjacent to distinct facets of η phase precipitates (Section 3.1), which directed attention to the crystallographic relationships between the phases. These relationships were investigated initially by searching reciprocal space for orientations in which both phases were near zone axes yielding small angle CBED patterns with coincident reflections. The investigation was then extended to consider numerous precipitates by employing automated orientation imaging based on scanning precession electron diffraction (SPED). This analysis assigns a crystallographic phase and orientation to each pixel in a scan by matching the PED pattern acquired at each position to a library of simulated patterns [40,41]. Indexation parameters and obtained quality maps are shown in the supplementary information (Table SI 4, Fig. SI 5,6). Here, we present the

orientations in the form of pole figures and visualise the disorientation between phases in axis-angle space [42–47]. In this space a disorientation is represented by a vector ρ:

$$\boldsymbol{\rho} = \omega\hat{\mathbf{n}}$$

where, $\hat{\mathbf{n}}$ is a unit vector parallel to the axis of rotation and, ω, is the angle of rotation [48]. This representation was preferred over other mappings [48], such as the commonly used Rodrigues vector, because the axes are in angular units, which simplifies direct interpretation. Further, we note that the differences between mappings are small for rotational angles <60°. For reference, various likely disorientations between the phases of interest are shown in this space in the supplementary information (Fig. SI 7).

3.5.1. Sigma phase orientation relationships

The crystallographic relationship between a σ phase precipitate and an adjacent η phase precipitate was determined using small angle CBED. The particular σ precipitate (Fig. 6) was situated on a large η phase facet and appeared to have grown along the grain boundary between two γ grains. Coincident zone axes were found to be: $[100]_\eta \parallel [110]_\sigma$ and $[210]_\eta \parallel [410]_\sigma$ and common reflections were found for the basal planes of the two phases.

The σ precipitate was also analysed using SPED in order to map the phases present and to determine the orientation of each crystal, represented as pole figures (Fig. 7). Poles were selected to highlight the crystallographic relationships and shared poles are marked with an asterisk on the pole figure. The relationship between η and σ was found to be:

Table 3
Phase composition summary for TCP phases in 718Plus (ˆLow energy peak (1.48 keV) — subject to absorption, ** = peak approaching noise limit).

at.%	Alˆ	Ti	Cr	Fe	Co	Nb	Ni	Mo	W
TCP1 C14	0.3	0.1**	24.8	11.5	16.1	5.7	26.7	9.7	5.2
TCP2 C14	0.4	0.1**	24.5	11.2	16.1	5.9	27.3	9.6	5.0
TCP3 C14	0.7	0.0**	26.0	11.2	14.9	5.2	29.1	8.7	4.3
TCP4 C14	0.8	0.2**	25.6	11.1	15.2	5.5	28.0	8.8	4.9
TCP5 σ	0.6	0.1**	52.2	10.1	11.2	0.3	19.9	4.2	1.6
TCP6 σ	0.1**	0.1**	52.1	10.2	10.3	0.1**	21.5	4.3	1.4

$$[100]_\eta \parallel [110]_\sigma$$

$$(001)_\eta \parallel (001)_\sigma$$

Further, automated analysis of the 4D SPED data set enabled crystallographic relationships between all phases in the region of interest to be determined routinely. In this particular case, the orientation relationship between σ phase and γ matrix was determined (Fig. 7d) $[011]_\gamma \parallel [140]_\sigma$, $(111)_\gamma \parallel (001)_\sigma$, as found previously [49,50].

Crystallographic relationships between five σ particles and their surrounding microstructure were compared by plotting the disorientation between phases in the appropriate fundamental zone of axis-angle space (Fig. 8). For each phase combination, 50 disorientations were calculated from the orientations associated with 50 randomly selected pixels in each phase. The calculated disorientations form a cluster in axis-angle space ca. 2° radius
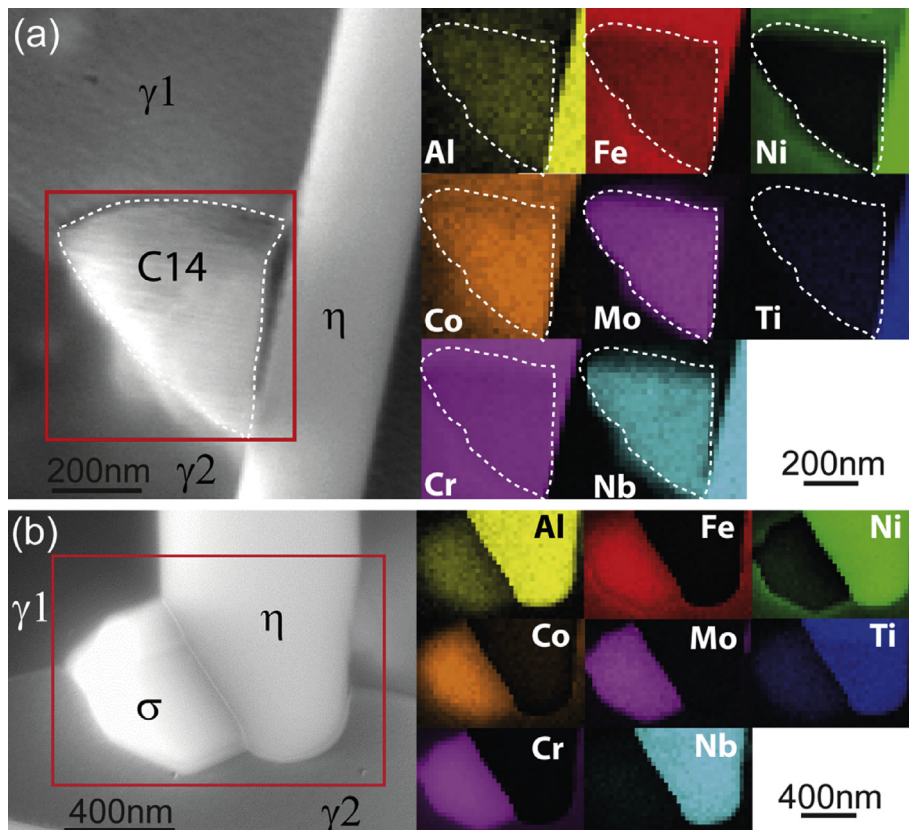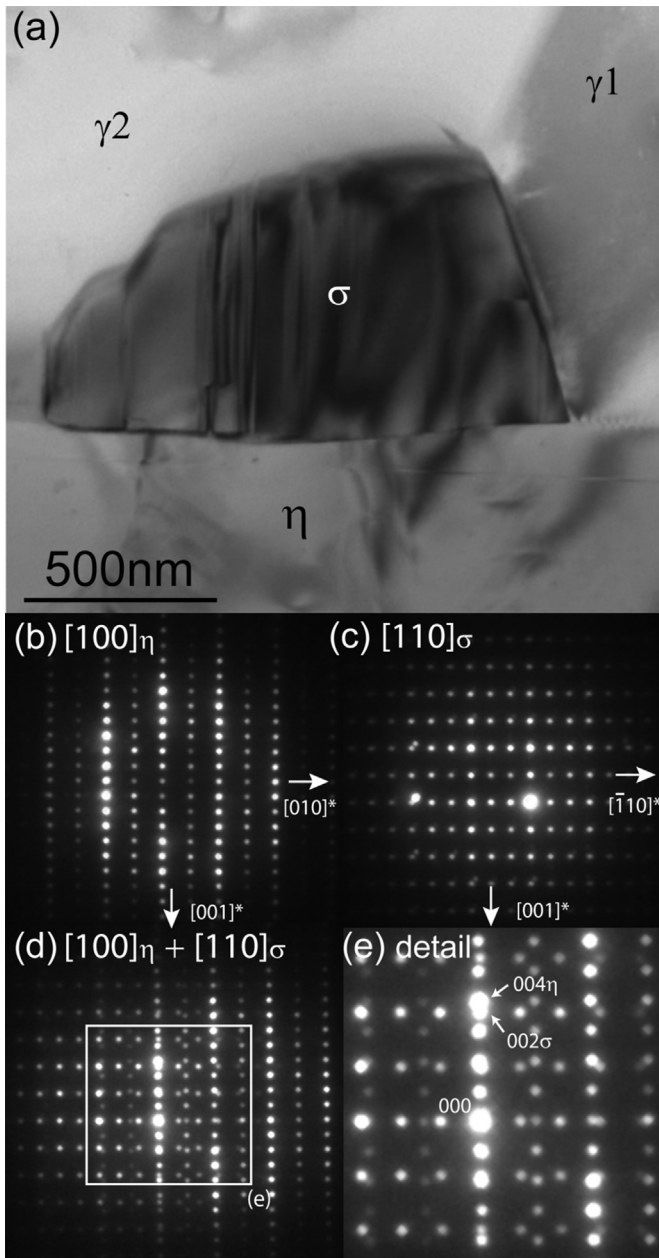

Fig. 5. ADF-STEM images and elemental maps from EDX spectrum images showing chemical segregation between (a) C14 Laves phase and (b) σ phase.

Fig. 6. (a) BF image showing σ precipitate and surrounding phases (b, c) single phase diffraction patterns for coincident zone axes and (d) a pattern taken across the interface showing both sets of reflections (e) detail thereof.

(supplementary section, Fig. SI 8), indicative of the level of uncertainty of the analysis. This is consistent with assessments of orientation precision made for spot based orientation determination [51–53]. The orientation relationships described thus far are marked with bounded yellow circles (detail Fig. 8a).

It was found that the η-σ orientation relationship, identified in the initial region of interest, occurred in two out of five cases and in the remaining three, the η-σ relationship did not indicate a strong crystallographic preference. On the other hand, in four out of five cases preference for the γ-σ relationship $[011]_\gamma \| [140]_\sigma$, $(111)_\gamma \| (001)_\sigma$ was observed. Four regions of interest fulfil the relationship as their clusters are situated close to the bounded yellow circle with one cluster situated about 5° away from the

relationship. An important feature of representing data in axis-angle space is the splitting of disorientation clusters when a bounding plane is crossed due to the symmetry operators [48]. This can be seen in Fig. 8a for a blue cluster on the top and purple clusters, one at the bottom and one at the back.

### 3.5.2. C14 Laves phase orientation relationships

The crystallographic relationships between two C14 Laves phase precipitates and the η phase precipitate to which they are both adjacent were determined using small angle CBED (Fig. 9). The C14 Laves precipitates are situated on either side of the η lath, surrounded by γ matrix and with one of the precipitates (#1) displaying significant intergrowth with the η phase. Both precipitates were found to have similar orientations and a single coincident pair of zone axes was found between the C14 Laves and η phase as well as a single common reflection indicating the following orientation relationship:

$$[210]_\eta \| [631]_{C14}$$

$$\left(\overline{1}21\right)_\eta \| \left(10\overline{6}\right)_{C14}$$

As with the σ phase, SPED was used to investigate the local microstructure around the C14 Laves precipitates. Fig. 10 shows the phases and the orientation of each crystal plotted as pole figures. A coincident pair of poles $\left(\overline{1}21\right)_\eta \| (10\overline{6})_{C14}$ was identified and indicated with an asterisk.

The crystallographic relationships between four C14 Laves phases and their surrounding microstructure are illustrated in axis-angle space in Fig. 11 following a procedure similar to that described for the σ precipitate in the previous section. Here, no
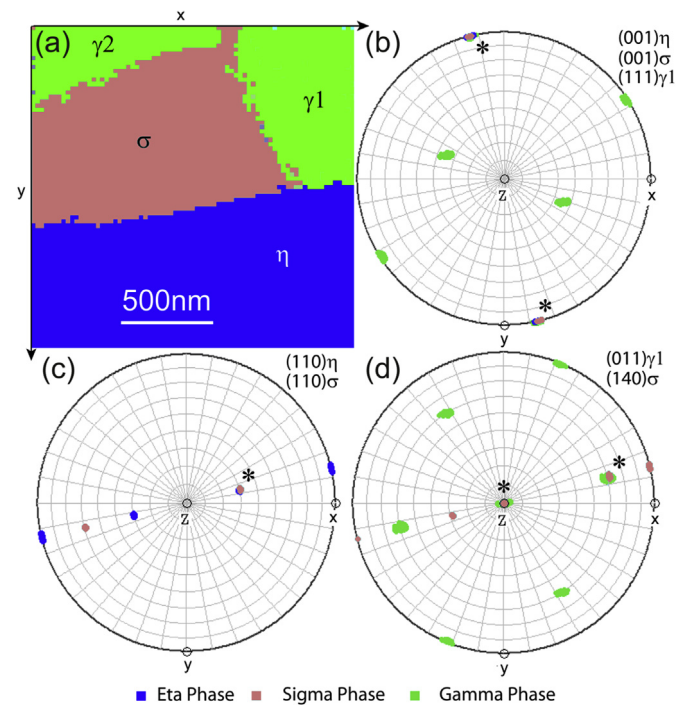
Fig. 7. (a) Phase map, produced from SPED data, showing the σ phase precipitate and surrounding microstructure (b–d) Pole figures showing important crystallographic poles. Note that in the η phase the $\{110\}_\eta$ poles are parallel to the $\langle 100 \rangle_\eta$ directions. * marks common poles.
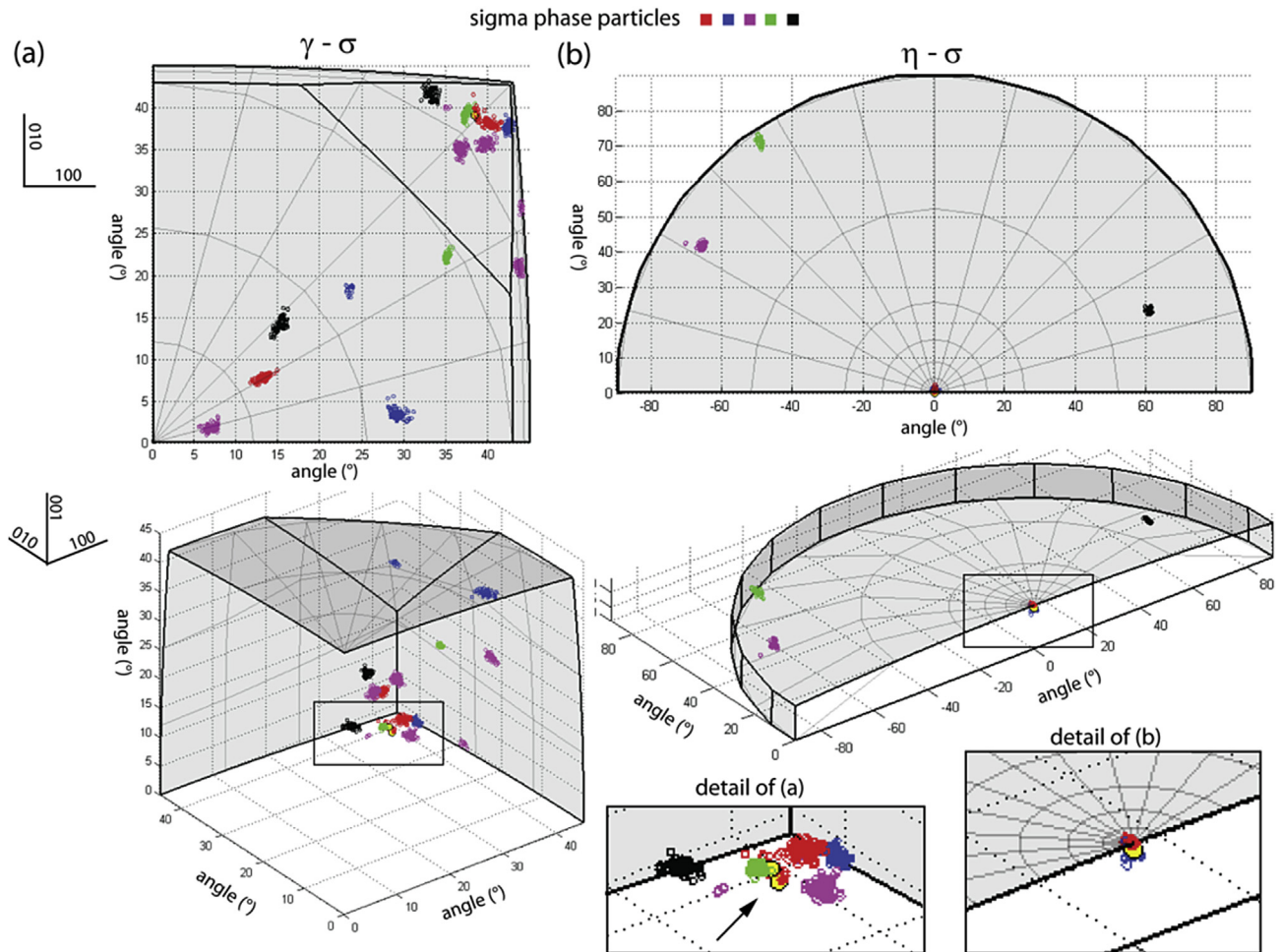
Fig. 8. Fundamental zones of axis-angle space with disorientations found in this study (a) for γ and σ phase (cubic-tetragonal combination) (b) for η and σ phase (hexagonal-tetragonal combination).
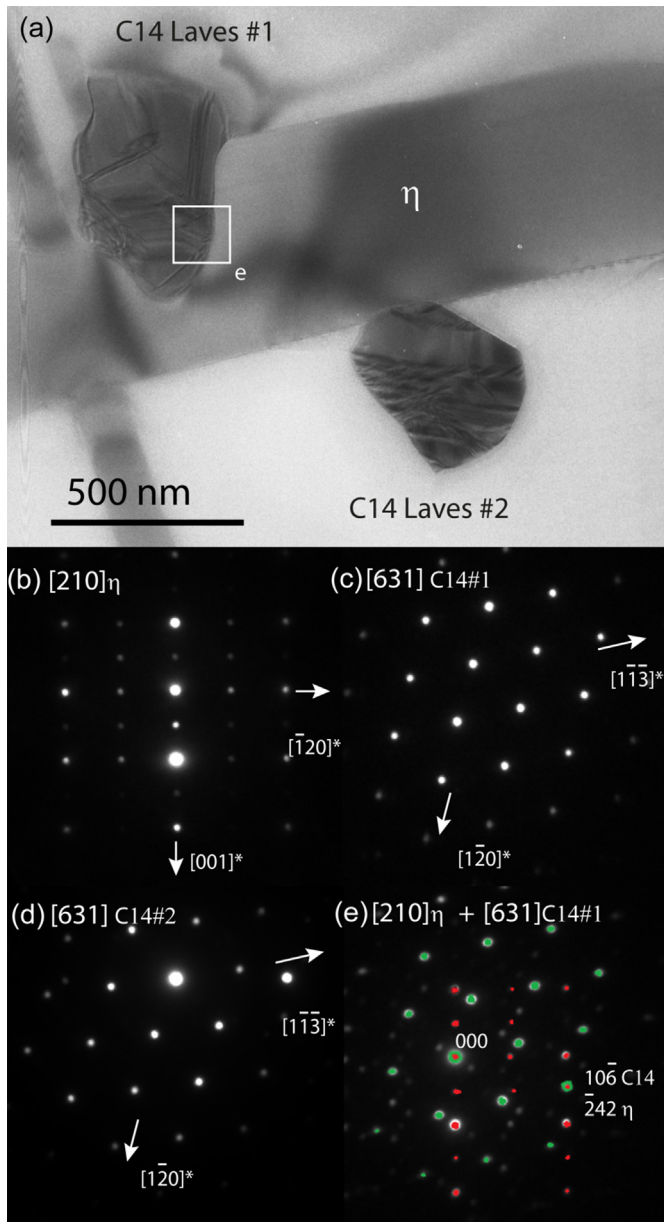
preferential crystallographic relationship is observed between the C14 Laves phase precipitates and either the η laths or γ matrix, in contrast to the findings for σ precipitates. Although a basal plane relationship may have been expected for these two hexagonal systems, the 6% lattice mismatch is likely to preclude any such simple relationship.

4. Discussion

We have shown that TCP phases form in 718Plus after relatively short annealing times (ca. 30 h). Previous experimental studies [24], have not seen this, perhaps because of the relatively small size and location of the TCP crystallites at the γ-η interface making them a challenge to identify. Laves and σ phase formation in 718Plus was recently predicted by thermodynamic modelling using JMatPro 6.0 [54] in a study on η phase precipitates [55]. No experimental evidence was presented in that work and our findings are consistent with this prediction. Of the TCP precipitates studied, approximately half were C14 Laves phase and half σ phase, although, one C36 Laves phase precipitate was also observed. These precipitates often occur at the γ-η interface on the facets of η particles, which may be expected due to chemical segregation associated with the η particles. We find that the TCP phases form with a narrow compositional range (Table 3), similar to the behaviour of binary Laves phases [31]. The enrichment trends are

also in line with compositions found for TCP particles in alloy 718 (supplementary information Table SI 3). No evidence has been found for α-Cr, the predominant co-precipitate of δ in 718 [37,56], which is surprising as Cr levels in 718Plus are relatively high. Which TCP phases form is likely to be a function of the availability of specific elements. The σ phase, for example, rejects Nb and Ni more so than the C14 Laves phase. It is therefore less likely to find suitable conditions at a matrix grain boundary but rather at the γ-η phase boundary, in line with our observations here showing all TCPs found at grain boundaries were C14 Laves phase.
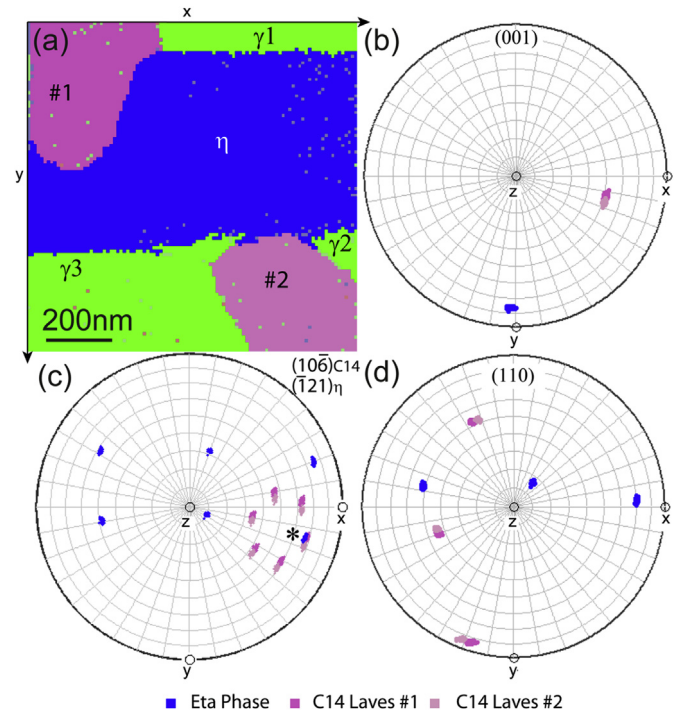
It is also assumed that stable nuclei will be sensitive to the degree of coherency at the interface, especially σ phase, which has been shown to grow in γ according to a distinct orientation relationship, matching up the close-packed planes. This preference has been found for all sites of interest studied. As has been pointed out before by Rae et al. [19] the lattice mismatch has a strong effect on the morphology of TCP precipitates in the γ matrix. They show that for a given alloy composition that leads to a good match σ phase forms sheets in the matrix. For other alloy composition with an increased mismatch, blocky precipitates are formed. In the light of these considerations, it seems plausible to assume that, in 718Plus, the σ phase has a greater mismatch with γ, as σ particles have a blocky morphology. This might also explain why the orientation relationship is not fulfilled closely, with deviations of up to about 3°.

Fig. 9. (a) BF TEM image showing two C14 Laves particles at opposite sides of an η precipitate (b–d) single phase patterns for coincident zone axes and (e) a pattern across the C14-η interface (from the region boxed in (a)) showing common reflections.

Fig. 10. (a) Phase map, produced from SPED data, showing the σ phase precipitate and surrounding microstructure (b–d) pole figures showing important crystallographic poles. *marks common poles.

ca. 6% might be too high for matching up basal planes between C14 Laves and η phase. The same would apply to C14 Laves and the close-packed γ matrix planes as the mismatch between η and γ is very small. Initially the finding of two C14 Laves particles with the same orientation on opposite sides of an η particle was assumed to be indicative of a strong orientation relationship (Fig. 9). However, additional sites of interest did not confirm this trend and so it may be that the two particles had been connected in the original sample, but that this connection was cut during the etching procedure.
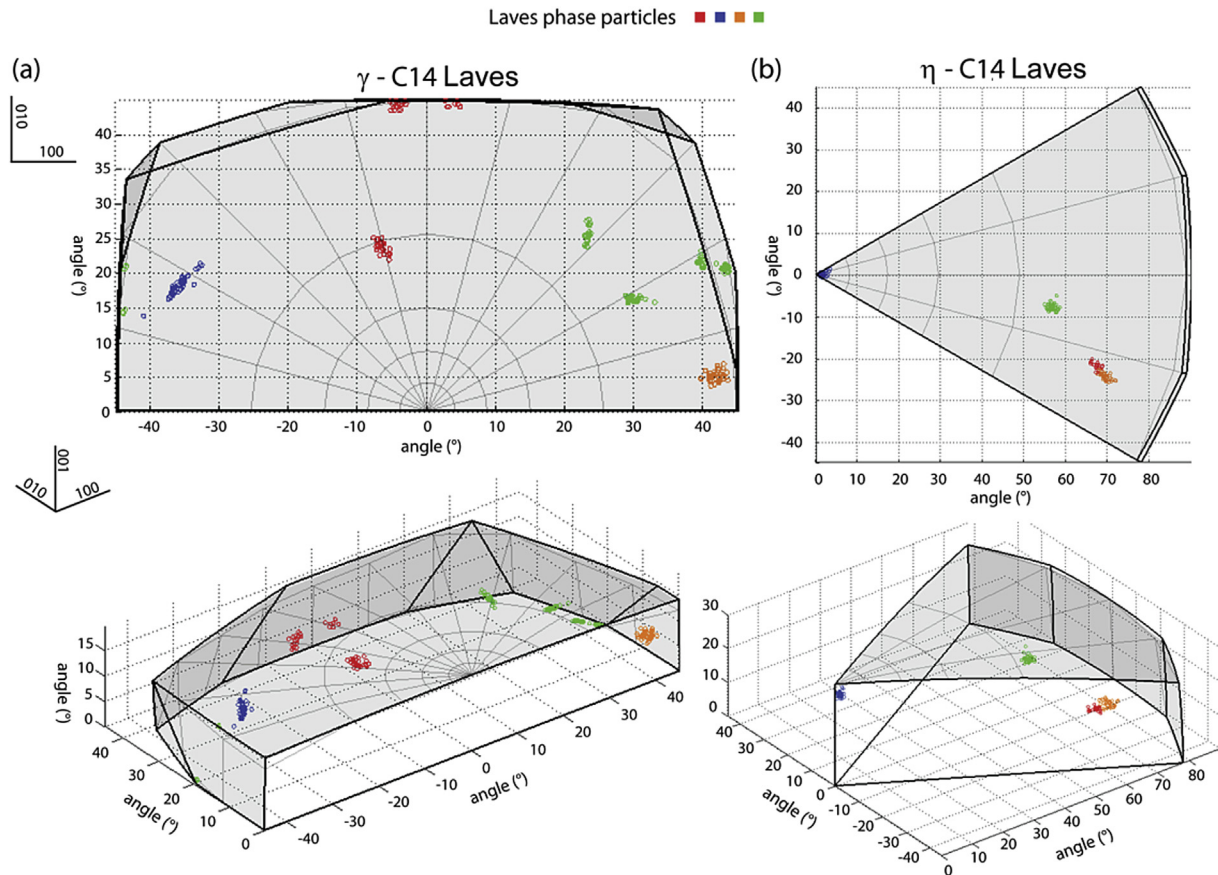
The observation of TCP phases after relatively short annealing times (ca. 30 h, condition A) has important implications for the prediction of constituent phases and long-term microstructural stability of 718Plus. It also highlights that the thermomechanical history of the alloy influences its stability and the morphology and extent of η phase formed [31,57], which can be altered through a change in processing route. As the γ matrix is depleted of solid solution elements by the formation of TCPs, it is reasonable to expect that there may be a detrimental effect on mechanical properties.

5. Conclusions

The following conclusions can be drawn from this work:

1. TCP phases were found in annealed conditions of the commercial nickel-based superalloy 718Plus.
2. The crystal structure and chemistry of TCP phases was found to be consistent with σ and C14 Laves phase. Both phases are enriched in Cr, Co, Fe, Ni and Mo with slightly higher levels of Cr in σ and additional Nb enrichment only in the C14 Laves phase.
3. C14 Laves and σ phase were found to nucleate mainly at distinct facets of thick η phase particles which are abundantly present in the microstructure examined.

The orientation relationship described between η and σ seems to be a consequence of a γ-η orientation relationship which has likely formed during forging and pre-solution treatment and therefore before any σ formation. If a σ precipitate grows on any of the four equivalent {111} planes in γ, then there is a 25% chance that it will also be in an orientation relationship with η, which is consistent with the ratio found in this study. In line with the above, in both occurrences of the orientation relationship, the η basal plane facet was the one occupied by σ. This suggests that certain η facets promote certain disorientations. However, the more significant orientation relationship that σ has is with γ as we have consistently found the same orientation relationship, which is also intuitive as σ grows into the γ grain.

Coherency, or the lack thereof, might also explain why no strong orientation relationship has been found for the C14 Laves phase with its surrounding microstructure. The basal plane mismatch of

Fig. 11. Fundamental zone of axis-angle space with disorientations found in this study (a) for γ and C14 Laves phase (cubic-hexagonal combination) (b) for η and C14 Laves phase (hexagonal-hexagonal combination).

4. The σ phase was found to nucleate with distinct disorientations with respect to the η phase, studied using SPED. According to SPED data the orientation of the surrounding γ phase also has a strong impact on the growth of σ phase.

5. BF and DF imaging confirmed the presence of planar faults in both TCP phases. At least two deformation mechanisms found in C14 Laves in 718Plus are noteworthy with defects giving rise to streaking along the [001]*, [011]* and [021]* directions. The second and third of these hint towards previously unreported deformation modes, consistent with deformation on the (011) and (021) planes, respectively.

Appendix A. Supplementary data

Supplementary data related to this article can be found at http://dx.doi.org/10.1016/j.actamat.2017.03.038.

References

[1] R. Jeniski, R.L. Kennedy, Nickel-base superalloy designed for aerospace, Adv. Mater. Process (2006) 19–22.

[2] W. Cao, R.L. Kennedy, Role of chemistry in 718-type alloys — Allvac ® 718Plus ™ alloy development, in: Superalloys 2004 (Tenth Int. Symp.), 2004.

[3] K.A. Unocic, R.W. Hayes, M.J. Mills, G.S. Daehn, Microstructural features leading to enhanced resistance to grain boundary creep cracking in Allvac 718Plus, Metall. Mater. Trans. A 41 (2009) 409–420, http://dx.doi.org/10.1007/s11661-009-0099-4.

[4] M. Sundararaman, P. Mukhopadhyay, S. Banerjee, Precipitation of the Ni3Nb phase in two nickel base superalloys, Metall. Trans. A 19 (1988) 453–465.

[5] J.F. Radavich, High temperature degradation of alloy 718 after longtime exposures, in: Superalloys 1992, 1992, pp. 497–506, http://dx.doi.org/10.7449/1992/Superalloys_1992_497_505.

[6] W. Cao, Solidification and solid state phase transformation of Allvac ® 718PLUS ™ alloy, in: Superalloy 718, 625, 706 Deriv. 2005, 2005, pp. 165–177.

[7] E.J. Pickering, H. Mathur, A. Bhowmik, O.M.D.M. Messé, J.S. Barnard, M.C. Hardy, et al., Grain-boundary precipitation in Allvac 718Plus, Acta Mater 60 (2012) 2757–2769, http://dx.doi.org/10.1016/j.actamat.2012.01.042.

[8] O.M.D.M. Messé, J.S. Barnard, E.J. Pickering, P.A. Midgley, C.M.F. Rae, On the precipitation of delta phase in Allvac ® 718Plus, Philos. Mag. 94 (2014) 1132–1152, http://dx.doi.org/10.1080/14786435.2013.878052.

[9] A. Casanova, N. Martín-Piris, M. Hardy, C.M.F. Rae, Evolution of secondary phases in alloy ATI 718Plus ® during processing, MATEC Web Conf. 14 (2014) 9003, http://dx.doi.org/10.1051/matecconf/20141409003.

[10] K. Löhnert, F. Pyczak, Microstructure evolution in the nickel base superalloy Allvac®718PlusTM, in: 7th Int. Symp. Superalloy 718 Deriv, 2010, pp. 877–891.

[11] J.F. Uginet, J.J. Jackson, Alloy 718 forging development for large land-based gas turbines, in: Superalloys 718, 625, 706 Deriv. 2005, 2005, pp. 57–67.

[12] D. Srinivasan, L.U. Lawless, E.A. Ott, Experimental determination of TTT dia-gram for ally 718PLUS®, in: Superalloys 2012 12th Int. Symp. Superalloys, 2012, pp. 759–768.

[13] X. Liu, J. Xu, E. Barbero, W. Cao, R.L. Kennedy, Effect of thermal treatment on the fatigue crack propagation behavior of a new Ni-base superalloy, Mater. Sci. Eng. A 474 (2008) 30–38, http://dx.doi.org/10.1016/j.msea.2007.05.033.

[14] A.S. Wilson, Formation and effect of topologically close-packed phases in nickel-base superalloys, Mater. Sci. Technol. 836 (2016) 1–11, http://dx.doi.org/10.1080/02670836.2016.1187335.

[15] S. Tin, T.M. Pollock, Phase instabilities and carbon additions in single-crystal nickel-base superalloys, Mater. Sci. Eng. A 348 (2003) 111–121, http://dx.doi.org/10.1016/S0921-5093(02)00637-8.

[16] K.R. Vishwakarma, N.L. Richards, M.C. Chaturvedi, Microstructural analysis of fusion and heat affected zones in electron beam welded Allvac® 718PLUS™ superalloy, Mater. Sci. Eng. A 480 (2008) 517–528, http://dx.doi.org/10.1016/j.msea.2007.08.002.

[17] K.R. Vishwakarma, N.L. Richards, M.C. Chaturvedi, HAZ microfissuring in EB welded Allvac 718Plus alloy, in: Superalloy 718, 625, 706 Deriv. 2005, 2005, pp. 637–648.

[18] K.R. Vishwakarma, O.A. Ojo, P. Wanjara, M.C. Chaturvedi, Linear friction welding of Allvac® 718Plus superalloy, in: 7th Int. Symp. Superalloy 718 Deriv, 2010, pp. 413–426.

[19] C.M.F. Rae, R.C. Reed, The precipitation of topologically close-packed phases in rhenium-containing superalloys, Acta Mater 49 (2001) 4113–4125, http://dx.doi.org/10.1016/S1359-6454(01)00265-8.

[20] C.M.F. Rae, M.S.A. Karunaratne, C.J. Small, R.W. Broomfield, C.N. Jones, R.C. Reed, Topologically close packed phases in an experimental rhenium-containing single crystal superalloy, in: Superalloys 2000, 2000, pp. 767–776. http://www.tms.org/superalloys/10.7449/2000/Superalloys_2000_767_776.pdf.

[21] B. Seiser, R. Drautz, D.G. Pettifor, TCP phase predictions in Ni-based superal-loys: structure maps revisited, Acta Mater 59 (2011) 749–763, http://dx.doi.org/10.1016/j.actamat.2010.10.013.

[22] M.G. Burke, M.K. Miller, Precipitation in alloy 718: a combined AEM and APFIM investigation, in: Superalloys 718, 625, 706 Deriv. 1991, 1991, pp. 337–350.

[23] O.A. Idowu, O.A. Ojo, M.C. Chaturvedi, Effect of heat input on heat affected zone cracking in laser welded ATI Allvac 718Plus superalloy, Mater. Sci. Eng. A 455 (2007) 389–397, http://dx.doi.org/10.1016/j.msea.2006.11.054.

[24] J.F. Radavich, T. Carneiro, A microstructural study of alloy 718PlusTM, in: Superalloys 718, 625, 706 Deriv. 2005, 2005, pp. 329–340.

[25] Nanomegas, ASTAR - Application Notes Nanoscale TEM Orientation Imaging Analysis, 2016, pp. 1–32. www.nanomegas.com.

[26] J.S. Barnard, D.N. Johnstone, P.A. Midgley, High-resolution scanning preces-sion electron diffraction: alignment and spatial resolution, Ultramicroscopy 174 (2017) 79–88, http://dx.doi.org/10.1016/j.ultramic.2016.12.018.

[27] CrystalMaker, 2016. www.crystalmaker.com/crystalmaker.

[28] SingleCrystal, 2016. www.crystalmaker.com/singlecrystal.

[29] A. Bhowmik, Refractory Metal Laves Phase Alloys Based on the Cr-Ta System (PhD Thesis, University of Cambridge), University of Cambridge, 2012.

[30] D.E. Luzzi, G. Rao, T.A. Dobbins, D.P. Pope, Deformation twinning at low temperatures in a Hf–V–Nb cubic laves phase, Acta Mater 46 (1998) 2913–2927, http://dx.doi.org/10.1016/S1359-6454(97)00418-7.

[31] K.S. Kumar, P.M. Hazzledine, Polytypic transformations in Laves phases, In-termetallics 12 (2004) 763–770, http://dx.doi.org/10.1016/j.intermet.2004.02.017.

[32] A. Bhowmik, H.J. Stone, Microstructure and mechanical properties of two-phase Cr-Cr2Ta alloys, Metall. Trans. A 43A (2012) 3283–3292, http://dx.doi.org/10.1016/S1006-706X(12)60088-0.

[33] A. Bhowmik, K.M. Knowles, H.J. Stone, Microstructural evolution and inter-facial crystallography in Cr-Cr2Ta, Intermetallics 31 (2012) 34–47, http://dx.doi.org/10.1016/j.intermet.2012.06.001.

[34] H.Q. Ye, D.N. Wang, K.H. Kuo, Domain structures of tetrahedrally close-packed phases with juxtaposed pentagonal antiprisms II. Domain boundary struc-tures of the C14 Laves phase, Philos. Mag. A 51 (1985) 849–856, http://dx.doi.org/10.1080/01418618508237592.

[35] M.F. Chisholm, S. Kumar, P. Hazzledine, Dislocations in complex materials,

[36] Science 307 (2005) 701–703, http://dx.doi.org/10.1126/science.1105962.

[36] F. de la Peña, T. Ostasevicius, V.T. Fauske, P. Burdet, P. Jokubauskas, M. Sarahan, et al., Hyperspy: HyperSpy 1.0.1, 2015, http://dx.doi.org/10.5281/zenodo.46897.

[37] S.T. Wlodek, R.D. Field, The effects of long time exposure on alloy 718, in: Superalloys 718, 625, 706 Deriv. TMS TMS, 1994, pp. 659–670, http://dx.doi.org/10.7449/1994/Superalloys_1994_659_670.

[38] S.J. Sijbrandij, M. Miller, J. Horton, W. Cao, Atom probe analysis of nickel-based superalloy IN-718 with boron and phosphorus additions, Mater. Sci. Eng. A 250 (1998) 115–119, http://dx.doi.org/10.1016/S0921-5093(98)00546-2.

[39] M.G. Burke, M. Miller, Grain boundary intermetallic phases in alloy 718, in: MRS Proc, 2011, pp. 215–218, http://dx.doi.org/10.1557/PROC-186-215.

[40] A.S. Eggeman, R. Krakow, P.A. Midgley, Scanning precession electron tomog-raphy for three-dimensional nanoscale orientation imaging and crystallo-graphic analysis, Nat. Commun. 6 (2015) 7267, http://dx.doi.org/10.1038/ncomms8267.

[41] R. Vincent, P.A. Midgley, Double conical beam-rocking system for measure-ment of integrated electron diffraction intensities, Ultramicroscopy 53 (1994) 271–282, http://dx.doi.org/10.1016/0304-3991(94)90039-6.

[42] Y. He, J.J. Jonas, Representation of orientation relationships in Rodrigues-Frank space for any two classes of lattice, J. Appl. Crystallogr. 40 (2007) 559–569, http://dx.doi.org/10.1107/S0021889807012770.

[43] Y. He, S. Godet, J.J. Jonas, Representation of misorientations in rodrigues-frank space: application to the bain, kurdjumov-sachs, nishiyama-wassermann and pitsch orientation relationships in the gibeon meteorite, Acta Mater 53 (2005) 1179–1190, http://dx.doi.org/10.1016/j.actamat.2004.11.021.

[44] R.J. Bennett, R. Krakow, A.S. Eggeman, C.N. Jones, H. Murakami, C.M.F. Rae, On the oxidation behavior of titanium within coated nickel-based superalloys, Acta Mater 92 (2015) 278–289, http://dx.doi.org/10.1016/j.actamat.2015.03.052.

[45] Y. He, J.J. Jonas, Maximum disorientation angles between crystals of any point groups and their corresponding rotation axes, J. Appl. Crystallogr. 41 (2008) 803–807, http://dx.doi.org/10.1107/S0021889808016373.

[46] G. Ibe, K. Luecke, Description of orientation distributions of cubic crystals by means of 3-D rotation coordinates, Texture 1 (1972) 87–98.

[47] A. Morawiec, Orientations and Rotations - Computations in Crystallographic Textures, Springer-Verlag Berlin Heidelberg, 2004, http://dx.doi.org/10.1007/978-3-662-09156-2.

[48] F.C. Frank, Orientation mapping, Metall. Trans. A 19 (1988) 403–408, http://dx.doi.org/10.1007/BF02649253.

[49] M. Lewis, Precipitation of (Fe, Cr) sigma phase from austenite, Acta Metall. 14 (1966) 1421–1428, http://dx.doi.org/10.1016/0001-6160(66)90162-3.

[50] J. Steeds, J. Manfield, Convergent Beam Electron Diffraction of Alloy Phases, Adam Hilger Ltd, 1984.

[51] S. Zaefferer, A critical review of orientation microscopy in SEM and TEM, Cryst. Res. Technol. 46 (2011) 607–628, http://dx.doi.org/10.1002/crat.201100125.

[52] A. Morawiec, E. Bouzy, H. Paul, J.J. Fundenberger, Orientation precision of TEM-based orientation mapping techniques, Ultramicroscopy 136 (2014) 107–118, http://dx.doi.org/10.1016/j.ultramic.2013.08.008.

[53] A. Morawiec, E. Bouzy, On the reliability of fully automatic indexing of elec-tron diffraction patterns obtained in a transmission electron microscope, J. Appl. Crystallogr. 39 (2006) 101–103, http://dx.doi.org/10.1107/S0021889805032966.

[54] JMatPro, 2012. http://www.sentesoftware.co.uk/1852.aspx.

[55] M. Wang, J. Du, Q. Deng, Z. Tian, J. Zhu, The effect of phosphorus on the microstructure and mechanical properties of ATI 718Plus alloy, J. Alloys Compd. (2017) 1–16, http://dx.doi.org/10.1016/j.jallcom.2017.01.145.

[56] J.W. Brooks, P.J. Bridges, Metallurgical stability of Inconel alloy 718, in: Su-peralloys 1988 (Sixth Int. Symp., Tms), 1988, pp. 33–42, http://dx.doi.org/10.7449/1988/Superalloys_1988_33_42.

[57] D. Huenert, M. Proebstle, A. Casanova, R. Schluetter, R. Krakow, M. Buescher, et al., ATI 718PLUS ® - new nickel based disc alloy and its capabilities, in: Superalloys 2016 13th Int. Symp. Superalloys, 2016, pp. 783–792.

[58] D.B. Williams, C.B. Carter, Transmission Electron Microscopy A Textbook for Materials Science, Springer, New York, 2009.